

## Accepted Manuscript

Title: Ionization of Acetonitrile

Authors: Michael A. Parkes, Kevin M. Douglas, Stephen D. Price

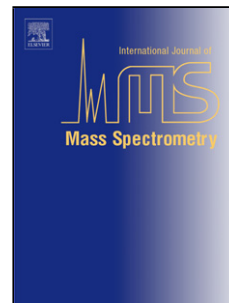
PII: S1387-3806(18)30305-1  
DOI: <https://doi.org/10.1016/j.ijms.2018.12.012>  
Reference: MASPEC 16107

To appear in: *International Journal of Mass Spectrometry*

Received date: 8 August 2018  
Revised date: 15 November 2018  
Accepted date: 14 December 2018

Please cite this article as: Parkes MA, Douglas KM, Price SD, Ionization of Acetonitrile, *International Journal of Mass Spectrometry* (2018), <https://doi.org/10.1016/j.ijms.2018.12.012>

This is a PDF file of an unedited manuscript that has been accepted for publication. As a service to our customers we are providing this early version of the manuscript. The manuscript will undergo copyediting, typesetting, and review of the resulting proof before it is published in its final form. Please note that during the production process errors may be discovered which could affect the content, and all legal disclaimers that apply to the journal pertain.



## Ionization of Acetonitrile

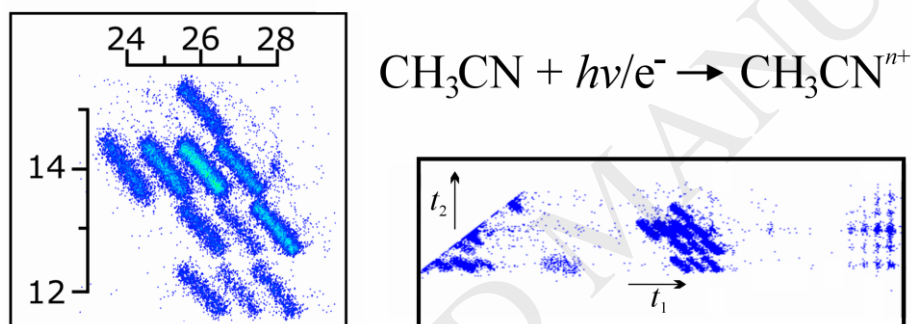
Michael A. Parkes\*, Kevin M. Douglas†, and Stephen D. Price\*

*Department of Chemistry, University College London, 20 Gordon Street, London, WC1H 0AJ,  
United Kingdom*

\*Corresponding authors: michael.parkes@ucl.ac.uk, s.d.price@ucl.ac.uk

† Current Address: School of Chemistry, University of Leeds, Leeds LS2 9JT UK.  
K.M.Douglas@leeds.ac.uk

### Graphical abstract



### Highlights:

- Precursor-specific partial ionization cross sections measured for  $\text{CH}_3\text{CN}$ .
- Decay routes and energetics of  $\text{CH}_3\text{CN}^{2+}$  determined.
- Comparison of photoionization (20-42 eV) and electron ionization (30-200 eV).

### Abstract

The ionization of acetonitrile has been studied using both electron and photon ionization combined with coincidence detection techniques. Relative partial ionization cross sections and relative precursor-specific partial ionization cross-sections are determined for all the cations formed

from single, double and triple electron ionization of  $\text{CH}_3\text{CN}$  from 30 – 200 eV electron energy. These cross sections characterize, distinguish and quantify the positive ions formed from these levels of ionization over the electron energy range investigated. To complement these electron ionization studies, relative ion yields for the formation of single ions (both monocations and dications) and monocation cation pairs have been measured following photoionization of  $\text{CH}_3\text{CN}$  from 20 – 42 eV using synchrotron radiation. There is a strong similarity between the photoionization data and electron ionization data.

### **Keywords**

electron ionization; photoionization; acetonitrile; ionization cross sections; dications; coincidence techniques

## 1. Introduction

Acetonitrile ( $\text{CH}_3\text{CN}$ ) is the smallest aliphatic nitrogen-containing hydrocarbon and finds extensive use as an industrial solvent.  $\text{CH}_3\text{CN}$  has been detected in the interstellar medium and is known to be important in various astrochemical processes.[1-3] Terrestrially  $\text{CH}_3\text{CN}$  is known to be formed in the atmosphere, where it is found in the stratosphere as  $\text{CH}_3\text{CN}(\text{H}_2\text{O})_n^+$  ions.[4-8] Acetonitrile has also been detected in the atmosphere of Titan.[9]  $\text{CH}_3\text{CN}$  is important in a medical context; for example, in breath analysis  $\text{CH}_3\text{CN}$  is a marker of the number of cigarettes a person smokes.[10]  $\text{CH}_3\text{CN}$  is also used as a chemical ionization agent in mass spectrometry to determine the position of double bonds in polyunsaturated fatty acids.[11] Knowing the position of these bonds is important to understand the effect of such fatty acids on human health.[12]

Due to the importance of  $\text{CH}_3\text{CN}$  in the various environments outlined above, many studies of its chemical and physical processes have been undertaken. These studies include work on the absorption of VUV photons,[13-18] interaction with metastable He,[19-22] electron ionization [23-26], modelling of the dissociation and rearrangement of  $\text{CH}_3\text{CN}^+$ [23,24,27] and dissociative ionization in femtosecond laser fields.[28]. However, quantitative studies of the electron ionization of  $\text{CH}_3\text{CN}$  are limited to measurements of yield curves and appearance energies.[23,26] A few studies have examined double ionization of  $\text{CH}_3\text{CN}$ . [29-35] Of these studies the majority have focussed on Auger processes at high-photon energies.[29-31] Of most relevance to the work reported in this paper is the study of the double ionization of  $\text{CH}_3\text{CN}$  by Ruhl *et al* who used He(II) radiation and coincidence methods to investigate the dissociation of  $\text{CH}_3\text{CN}^{2+}$ . [35] As a consequence of Ruhl *et al.*'s study, the formation of  $\text{H}_3^+$  from double ionization of  $\text{CH}_3\text{CN}$ , and other organic molecules, has been considered as a source of  $\text{H}_3^+$  in the interstellar medium.[32,34]

This paper reports a quantitative study of the electron ionization of  $\text{CH}_3\text{CN}$  from 30 – 200 eV using time-of-flight mass spectrometry coupled with coincidence detection. Relative cross sections are determined which quantify the formation of fragment ions and the level of ionization (single, double, triple) generating these individual ions. These cross sections are used to account for the decay processes of the  $\text{CH}_3\text{CN}^{2+}$  ion. To support this work, and investigate any differences between the consequences photoionization and electron ionization, we also present the results of coincidence experiments probing the photoionization of  $\text{CH}_3\text{CN}$  from 20 – 42 eV using synchrotron radiation.

## 2. Experimental

### 2.1 Electron Ionization

The electron ionization experiments reported here were performed using a time-of-flight mass spectrometer (TOFMS) running in a coincidence detection mode. Details of this apparatus have been presented previously and so only an outline of its operation will be given here.[36,37] Briefly, the

experiment is controlled by a pulse generator running at 50 kHz. The generator first triggers a home-built electron gun to produce a pulsed beam of electrons (the pulse duration is approximately 30 ns). This pulsed electron beam crosses the source region of the TOFMS where it interacts with the target gas. The target gas effuses continuously from a needle orientated at  $90^\circ$  to the path of the electron pulse. Both the electron beam and jet of target gas are oriented perpendicularly to the major axis of the TOFMS. Once the electron pulse has traversed the source region of the TOFMS, a voltage of +400 V is applied to the mass spectrometer's repeller plate. This voltage accelerates any ions formed by the electron pulse into the acceleration region of the TOFMS and on into the drift region. At the end of the drift region the ions impact on a detector comprised of a pair of microchannel plates. Signals from the detector are amplified, discriminated and registered as stop signals on a fast time-to-digital convertor (TDC). The start pulse for the TDC is sent by the pulse generator after it triggers the repeller plate pulse. The TDC records the flight times of up to three ions for every start it receives. The events recorded by the TDC are accumulated in a memory module followed by periodic transfer to a PC.

For all measurements reported here the sample pressure inside the TOFMS was maintained at  $10^{-6}$  Torr as recorded by an ion gauge. Use of these low pressures, combined with the low electron beam currents, ensures that on average there is considerably less than one ionizing event per electron pulse. This low event rate ensures that only a very small number of false coincidences arise in our data. These false coincidences can be easily removed using an autocorrelation function as described in more detail below.[36] To ensure that we can extract quantitative data from our experiments we have identified a set of conditions under which no intrinsic discrimination in our ion detection electronics is observed.[36] Further, the accelerating voltages of the TOFMS are such that all ions will reach the detector if they have less than 10 eV translational energy. As most dication dissociations involve total kinetic energy releases (KERs) that are less than 9 eV, the vast majority of ions formed from double ionization will be detected in our apparatus.[38] Ions with significant translational energies, formed by triple (and higher) ionization, can have KERs  $> 10$  eV. A proportion of these high kinetic energy ions may not reach the detector, hitting the walls of the flight tube. However, these losses can easily be corrected for by examining the form of the coincidence signals, as described below.[39]

### 2.1.1 Data Reduction

The coincidence data we record are classified as a function of the number of ions detected following each repeller plate pulse. Events involving the detection of only a single ion are added to a 'singles' mass spectrum, a simple histogram of time-of-flight versus ion counts. The relative ion intensities for monocations and dications in the singles spectrum,  $I[X^+]$  and  $I[X^{2+}]$ , are extracted from these spectra by evaluating the counts in each peak after applying a correction for the small, but

nonzero, baseline. A further correction is made for the small contribution to ion peaks (e.g. for  $\text{N}^+$  at  $m/z = 14$  amu) arising from residual air and water in the background gas in the vacuum chamber.[36]

Events with two or three ions detected per repeller pulse are termed either ‘pairs’ or ‘triples’. The pairs data are visualised as a 2D histogram with the number of counts plotted as a function of the flight times ( $t_1, t_2$ ) of both ions in the pair. In such pairs spectra different decay channels of a multiply-charged ion appear as distinct peaks. The relative intensity of each dissociation channel is then determined by summing the counts in each of these ‘pairs peaks’. As described earlier, despite the low event rates, the peaks in the pairs spectrum contain a small contribution due to false coincidences. The number of these false coincidences are evaluated, using a methodology involving the autocorrelation function of the singles mass spectrum, and subtracted on a peak by peak basis; this procedure has been described in the literature.[36,40] Any contribution to the recorded ion pairs from the residual air and water in the vacuum chamber can easily be evaluated and subtracted.[36] A further correction is made for those ion pairs where  $t_1$  and  $t_2$  are very similar, for example  $\text{H}^+ + \text{H}^+$ . For such dissociations it is necessary to allow for the loss of ion pairs due to the deadtime of the detection electronics. Specifically, the dead time of the detection electronics used in these experiments is approximately 32 ns. Thus, coincidences are missed if  $|t_1 - t_2| < 33$  ns. Fortunately, such losses can be easily estimated by extrapolating the visible part of the pairs peak back to  $t_1 = t_2$ . [36] The corrected intensities of each pairs peak that contains an  $\text{X}^+$  ion are then summed to produce the contribution of a fragment ion to the pairs spectrum,  $P[\text{X}^+]$ .

The triples data is analysed by first specifying the TOF range of an ion of interest ( $t_1$ ) and then finding all ion triples that contain at least one ion that lies in this TOF range. From this selected list of triples the times of the other two ions ( $t_2$  and  $t_3$ ) are plotted in a 2D histogram of their arrival times. This 2D triples spectrum is then analysed in the same manner as the pairs spectrum to produce  $T[\text{X}^+]$ , the contribution of a fragment ion ( $\text{X}^+$ ) to the triples spectrum.

From the values of  $I[\text{X}^+]$ ,  $I[\text{X}^{2+}]$ ,  $P[\text{X}^+]$ , and  $T[\text{X}^+]$  obtained from the experiment, the relative partial ionization cross-sections (PICS)  $\sigma_r[\text{X}^{m+}]$  (branching ratios) for forming each fragment ion can be derived. In addition we can also extract from our data the relative *precursor-specific* PICS,  $\sigma_n[\text{X}^{m+}]$ . The values of  $\sigma_r[\text{X}^{m+}]$  quantify how likely an  $\text{X}^{m+}$  ion is to be formed from an electron-acetonitrile collision at a given electron energy. The precursor-specific values  $\sigma_n[\text{X}^{m+}]$  breakdown the value of  $\sigma_r[\text{X}^{m+}]$  into the contribution to the yield of  $\text{X}^{m+}$  from single ( $n = 1$ ), double ( $n = 2$ ) and triple ( $n = 3$ ) ionization. For example, in the dataset presented in this paper,  $\sigma_r[\text{H}^+]$  quantifies the yield of  $\text{H}^+$  from all levels of ionization of  $\text{CH}_3\text{CN}$ ; whilst  $\sigma_1[\text{H}^+]$ ,  $\sigma_2[\text{H}^+]$  and  $\sigma_3[\text{H}^+]$  quantify the cross-sections for formation of  $\text{H}^+$  from single, double and triple ionization of  $\text{CH}_3\text{CN}$  respectively. For this study,  $\sigma_r[\text{X}^+]$  and  $\sigma_r[\text{X}^{2+}]$  are determined from the ion intensities using Eq. (1) and (2) while

Eq. (3) is an example of an equation derived to calculate a relative precursor-specific PICS (in this case  $\sigma_1[X^+]$ ):

$$\sigma_r[X^+] = \frac{I[X^+] + P[X^+] + T[X^+]}{I[\text{CH}_3\text{CN}^+]} \quad (1)$$

$$\sigma_r[X^{2+}] = \frac{I[X^{2+}]}{I[\text{CH}_3\text{CN}^+]} \quad (2)$$

$$\sigma_1[X^+] = \frac{I[X^+] + ((1 - f_i)f_i)P[X^+] + ((1 - f_i)^2 f_i^2)T[X^+]}{I[\text{CH}_3\text{CN}^+]} \quad (3)$$

In Eq. (3),  $f_i$  is the ion detection efficiency. Values of  $f_i$  lie between zero and unity due to ion losses at the grids in the TOFMS and the performance of the detector and associated electronics. Once  $f_i$  is known,  $f_i = 0.256$  for this work,  $\sigma_n[X^{m+}]$  can be evaluated. Full details of the methods used to determine  $f_i$  and to calculate the various relative PICS are given in a previous publication.[36]

In this study there are a number of potential product ions which have the same mass-to-charge ratio: for example an ion with  $m/z = 27$  could arise from  $\text{C}_2\text{H}_3^+$  or  $\text{HCN}^+$ . In this study we cannot always unambiguously distinguish the contributing ions at  $m/z$  values of: 14 ( $\text{N}^+$ ,  $\text{CH}_2^+$ ), 15 ( $\text{NH}^+$ ,  $\text{CH}_3^+$ ), 26 ( $\text{C}_2\text{H}_2^+$ ,  $\text{CN}^+$ ) and 27 ( $\text{C}_2\text{H}_3^+$ ,  $\text{HCN}^+$ ). However, when we are looking at ion pairs and triples, it is often possible to distinguish these ions. For example,  $\text{H}^+$  is detected in a pair together with an ion of  $m/z = 15$ . This  $m/z = 15$  ion must be the  $\text{NH}^+$  ion as there are not enough H atoms available in the parent  $\text{CH}_3\text{CN}$  to give rise to  $\text{H}^+ + \text{CH}_3^+$ . Therefore, where possible, we report data for these specific ions but in a few cases we report cross sections for a given mass, without identifying the ion.

The behaviour of several of the relative cross sections measured in this study reveal ionization thresholds within the range of electron energies we have employed. To estimate the energy of such ionization thresholds ( $E_A$ ), a threshold function  $f(E)$  has been fitted to the appropriate relative PICS in the threshold region[41]:

$$f(E) = \begin{cases} E < E_A : & b \\ E \geq E_A : & b + c(E - E_A)^P \end{cases} \quad (4)$$

In this threshold function,  $E$  is the photon or electron energy,  $b$  is the background signal below the energy threshold of a process,  $c$  and  $P$  are fitted parameters. For the majority of the thresholds analysed in this work  $P$  was found to lie close to unity.

In addition to the relative PICS, our coincidence data also reveals information characterizing the dynamics and energetics of the fragmentation of the multiply charged ions that are formed following electron ionization of acetonitrile. For example, the gradient of a peak in the pairs spectrum, the slope of the major axis of the lozenge shaped peak in a plot of  $t_1$  against  $t_2$  for that reaction (see inset in Figure 1), characterizes the correlation between the fragment ion momenta in the dissociation reaction associated with that peak. These peak gradients, extracted with a weighted least squares analysis, and

the shape of the coincidence peak in the pairs spectrum (Figure 1), can provide information on the mechanism of a given fragmentation.[42] For example, the ionic products of a two-body dicationic dissociation will have equal and opposite momenta, giving rise to a peak in the pairs spectrum with a gradient of -1. However, further dissociations of these primary products will lead to changes in the product momenta which will move the peak gradient away from -1, the precise value of the gradient depending on the ratio of the masses of the nascent ion and the dissociation product.[42] Thus, the gradient of a particular peak in the pairs spectrum can reveal the dissociation mechanism of the parent dication. More sophisticated analysis of the shape of such coincidence peaks, to determine far more detailed information on the dissociation mechanism of the dication, is possible in experiments with higher temporal resolution.[43,44] In the coincidence spectra presented in this study, the finite duration of the electron pulse restricts our analysis of the coincidence peak shapes to simple measurement of the peak gradients.

Plotting a TOF difference spectrum, intensity against  $(t_2 - t_1)$ , for a detected ion-pair can be used to determine the KER involved in the fragmentation that gives rise to that fragmentation. Individual fragmentation reactions typically generate a square peak in such a difference spectrum and the width of these square peaks is principally controlled by the KER. We extract estimates of the KER from these difference spectra by modelling their form using a Monte-Carlo simulation, including all the apparatus parameters.[36] From the value of the KER for a given dissociation channel, and the energies of the dissociation products, we can estimate the energy of the dicationic precursor,  $E_P(\text{CH}_3\text{CN}^{2+})$ , that dissociates into the ion pair of interest. Such an estimate requires a knowledge of the relative energies of the dissociation products  $E_{frag}$ :

$$E_P(\text{CH}_3\text{CN}^{2+}) = \text{KER} + E_{frag} \quad (5)$$

In making such an estimates of dicationic precursor energies, we commonly have to assume that the dissociation products are formed in their ground electronic states.

## 2.2 Photon Ionization

To support the electron ionization data, experiments on the photon ionization of  $\text{CH}_3\text{CN}$  were performed at the Swiss Light Source (SLS) synchrotron on the VUV beamline.[45] These experiments used the existing iPEPICO (*imaging PhotoElectron PhotoIon CO*incidence) endstation. The operation of this endstation has been described in detail in the literature.[46,47] The iPEPICO apparatus is designed to detect, in coincidence, the photoelectrons and photoions formed following photoionization. There are two detectors, one for electrons and one for ions, aligned opposite each other across a small (11 mm) interaction region. In this interaction region a beam of effusive gas is crossed by a pulsed beam of VUV photons from the beamline monochromator. Any second-order light from this monochromator is suppressed by an in-line noble gas filter.[48] Any electrons and

ions formed by ionization are extracted by a small continuous voltage into their respective detection regions. The fields in the electron detection region are chosen to achieve velocity map imaging and to discriminate strongly in favour of low-energy electrons. Specifically, only those electrons with energy  $<800$  meV will be focussed to the detector face, although there will still be a small contribution to the electron signal from those high-energy electrons whose initial velocities are aligned directly towards the detector. This high-energy contribution can be efficiently removed using a simple geometric correction scheme.[46] The electron detector employed is a position-sensitive detector, of the delay-line anode type, situated behind a multichannel plate arrangement. The ions are extracted into a standard TOFMS and detected using a multi-channel plate. The start signal of the detection system is provided by the detection of an electron.

Considering the energy balance following double photoionization of  $\text{CH}_3\text{CN}$ , we have:

$$h\nu = E(\text{CH}_3\text{CN}^{2+}) + \text{DIE} + \text{KE}_{e1} + \text{KE}_{e2} \quad (6)$$

Here,  $h\nu$  is the ionizing photon's energy,  $E(\text{CH}_3\text{CN}^{2+})$  is the double ionization energy required to populate a particular electronic state of the acetonitrile dication and  $\text{KE}_{e1/2}$  represents the kinetic energy of each of the two emitted electrons. An issue with using the iPEPICO apparatus to study double ionization is that only a single electron can be detected from each ionization event. However, as the photon energy passes through a double ionization threshold two very low energy electrons will be formed, and one of these electrons will be efficiently detected by the electron detector. Thus a signal corresponding to double ionization thresholds will appear in the coincidence spectra.

Two types of photoionization spectra were recorded to study the double photoionization of  $\text{CH}_3\text{CN}$ . The first class of spectrum is a photoelectron-photoion-coincidence (PEPICO) dataset. For these spectra coincidences between a threshold electron and a single ion were recorded as a function of photon energy over a range of 20 – 34 eV, with a standard step-size of 0.1 eV. In regions of the spectra where a threshold, the appearance of a new ion signal, was observed as the photon energy increased, spectra were repeated with a smaller photon energy step-size. From these PEPICO spectra it is possible to determine thresholds for the formation of monocations from single photoionization and dications from double photoionization. The thresholds are determined by fitting the PEPICO signal to the threshold law outlined above in Eq. ((4). For the PEPICO spectra recorded in this study, only ions coincident with electrons which hit the centre of the electron detector face have been used for determination of ion yields. Taking just this portion of the coincidences reduces influence of any energetic electrons on the results.[46] All ion intensities are reported relative to the signal of  $\text{CH}_3\text{CN}^+$ .

The second class of spectrum we record is a photoelectron-photoion-photoion coincidence (PEPIPICO) spectrum. In these measurements coincidences between a threshold electron and two monocations produced from double photoionization were recorded. Given the significant time

required to record PEPICO spectra with a satisfactory signal-to-noise ratio, the PEPICO spectra were measured between 34 and 42 eV at 1 eV intervals.

The PEPICO experiments record both pair events, where two ions are detected in coincidence with an electron, and singles events where just one ion is detected. As with the electron ionization experiments, the singles events are histogrammed to form a mass spectrum whilst the pairs data are visualised with a 2D histogram of the flight times ( $t_1, t_2$ ) of both ions in the pair. These two spectra (singles and pairs) are analysed in the same way as the electron ionization results (see above) to produce the ion intensities for monocations and dications in the singles spectrum,  $I[X^+]$  and  $I[X^{2+}]$  and the ion intensities for monocation pairs in the pairs spectrum  $P[Y^+ + Z^+]$ . The intensity of ions and ion pairs as a function of photon energy are reported as relative ion intensities (RII), relative to the  $\text{CH}_3\text{CN}^+$  signal, and used to reveal ionization thresholds.

### 3. Results

The electron ionization of  $\text{CH}_3\text{CN}$  was studied over a range of electron energies from 30 – 200 eV. A representative pairs spectrum and representative mass spectra are shown in Figure 1. The resulting data sets were analysed as described above to produce relative PICS,  $\sigma_r[X^{m+}]$  (Figure 22), and relative precursor-specific PICS,  $\sigma_1[X^+]$  (Figure 33),  $\sigma_2[X^+]$  (Figure 44) and  $\sigma_2[X^{2+}]$  (Figure 55) for electron ionization of  $\text{CH}_3\text{CN}$ . All cross-sections are reported relative to the formation of  $\text{CH}_3\text{CN}^+$  as indicated in Eq. (1)-(3). Values for  $\sigma_3[X^+]$  were also generated, however, due to their significant statistical uncertainty they are only reported in a tabulated form (Table S8) in the supplementary information (SI). Tabulated versions of all the relative cross-sections, with their associated uncertainty are also available in the SI.

Upon electron ionization of  $\text{CH}_3\text{CN}$  twenty two ions were detected in the singles, pairs and triples spectra;  $\text{H}^+$ ,  $\text{H}_2^+$ ,  $\text{H}_3^+$ ,  $\text{C}^{2+}$ ,  $\text{C}^+$ ,  $\text{CH}^+$ ,  $\text{CH}_2^+ / \text{N}^+$ ,  $\text{CH}_3^+ / \text{NH}^+$ ,  $\text{C}_2\text{N}^{2+}$ ,  $\text{C}_2\text{HN}^{2+}$ ,  $\text{C}_2\text{H}_2\text{N}^{2+}$ ,  $\text{CH}_3\text{CN}^{2+}$ ,  $\text{C}_2^+$ ,  $\text{C}_2\text{H}^+$ ,  $\text{C}_2\text{H}_2^+/\text{CN}^+$ ,  $\text{C}_2\text{H}_3^+/\text{CHN}^+$ ,  $\text{CH}_2\text{N}^+$ ,  $\text{CH}_3\text{N}^+$ ,  $\text{C}_2\text{N}^+$ ,  $\text{C}_2\text{HN}^+$ ,  $\text{C}_2\text{H}_2\text{N}^+$  and  $\text{C}_2\text{H}_3\text{N}^+$ . We note that no signals due to  $\text{N}^{2+}$  ions were observed. In total, forty five different dissociation reactions forming ion pairs were detected, with eleven different channels forming ion triples appearing at higher ionization energies. The complete lists of ion pairs and ion triples detected following electron ionization are given in the SI.

The photon ionization of  $\text{CH}_3\text{CN}$  was investigated over a photon energy range from 20 – 42 eV. PEPICO spectra were recorded from 20 – 36 eV and PEPICO spectra were recorded from 33 – 42 eV. Representative PEPICO spectra are shown in Figure 66. In these photoionization experiments at the SLS twenty three different ions were detected;  $\text{H}^+$ ,  $\text{H}_2^+$ ,  $\text{H}_3^+$ ,  $\text{C}^{2+}$ ,  $\text{N}^{2+}$ ,  $\text{C}^+$ ,  $\text{CH}^+$ ,  $\text{CH}_2^+ / \text{N}^+$ ,  $\text{CH}_3^+ / \text{NH}^+$ ,  $\text{C}_2\text{N}^{2+}$ ,  $\text{C}_2\text{HN}^{2+}$ ,  $\text{C}_2\text{H}_2\text{N}^{2+}$ ,  $\text{C}_2\text{H}_3\text{N}^{2+}$ ,  $\text{C}_2^+$ ,  $\text{C}_2\text{H}^+$ ,  $\text{C}_2\text{H}_2^+/\text{CN}^+$ ,  $\text{C}_2\text{H}_3^+/\text{CHN}^+$ ,  $\text{CH}_2\text{N}^+$ ,  $\text{CH}_3\text{N}^+$ ,  $\text{C}_2\text{N}^+$ ,  $\text{CHCN}^+$ ,  $\text{CH}_2\text{CN}^+$  and  $\text{CH}_3\text{CN}^+$ . forty five different ion pairs were observed and are listed in the SI.

## 4. Discussion

### 4.1 Electron Ionization

The values of  $\sigma_r$  we have derived from our CH<sub>3</sub>CN electron ionization data are shown in Figure 2. As the electron energy is increased the relative PICs all show the same trend: a rise to a peak value before gradually decreasing as the electron energy is increased further. Such behaviour is often observed for such relative electron ionization cross-sections.[36,37,39,49-52] All the monocation products from single electron ionization of CH<sub>3</sub>CN detected in this experiment have non-zero  $\sigma_1$  values at 30 eV (the lowest electron energy used in this study), indicating that all the thresholds for the formation of these ions by single ionization lie below 30 eV.

In contrast, for all the ions we detect the values of  $\sigma_2$  are zero, within the experimental error bar, at 30 eV. However, at 35 eV, several of the ions show non-zero  $\sigma_2$  values (Figure 44 and Figure 55). This observation shows that the double ionization energy (DIE) of CH<sub>3</sub>CN, the energy required to populate the ground state of the dication, lies between 30 and 35 eV, consistent with the DIE of CH<sub>3</sub>CN of  $33.3 \pm 0.3$  eV, measured using charge-transfer spectroscopy.[33] The energetic thresholds ( $E_A$ ) for ions formed *via* double ionization of CH<sub>3</sub>CN were determined by fitting the  $\sigma_2$  values just above the threshold, as described above (Eq. ((4))), and are given in Table 1. The majority of monocation and dication products from double ionization of CH<sub>3</sub>CN have thresholds in the 35 – 45 eV energy range. Our value of the energetic threshold for the generation of CH<sub>3</sub>CN<sup>2+</sup>, of  $34.1 \pm 0.8$  eV (Table 1) is in accord with the value of the DIE determined by Bayliss *et al* ( $33.3 \pm 0.3$  eV) using charge-transfer spectroscopy.[33]

Table 2 lists the KERs we determine for the observed ion pairs which are formed *via* a two-body mechanism and which have a significant enough intensity to allow reliable analysis. As shown in Table 2, we have extracted the KER for each channel at the lowest electron energy for which there are statistically reliable signals. From the KERs we have derived dication precursor-state energies, which are also listed in Table 2. All the precursor energies in Table 2 have been determined assuming the ionic products are formed in their ground electronic states. The data in Table 2 shows that all the two-body dissociations of CH<sub>3</sub>CN<sup>2+</sup> forming CH<sub>2</sub>CN<sup>+</sup> + H<sup>+</sup> and CHN<sup>+</sup> + CH<sub>2</sub><sup>+</sup> originate from low down in the manifold of CH<sub>3</sub>CN<sup>2+</sup> states, perhaps from the ground state, whereas the formation of CHCN<sup>+</sup> + H<sub>2</sub><sup>+</sup> occurs from a state (or states) with significant (4 eV) internal excitation. Indeed, the calculations of Bayliss *et al* show that there are a large number of CH<sub>3</sub>CN<sup>2+</sup> electronic states in this energy region.[33] The KERs we extract for the dissociation of CH<sub>3</sub>CN<sup>2+</sup> to CH<sub>2</sub>N<sup>+</sup> + CH<sup>+</sup> or to CN<sup>+</sup> + CH<sub>3</sub><sup>+</sup> result in dicationic precursor energies close to 31 eV, below the DIE of 33.3 eV. Such low precursor energies could indicate that the products of these dissociations are not formed in their ground electronic states. Alternatively, as has been observed before for other molecules, the threshold

of the two-body dissociation could originate from the dissociation of excited monocation states,  $\text{CH}_3\text{CN}^{+*}$ , lying below the DIE.[53-59] These excited monocation states, which are perhaps part of a Rydberg series converging on the close-lying dicationic states, fragment into a monocation and an electronically excited neutral, with the neutral subsequently autoionizing to form the second monocation detected. As is well-established, this mechanism could generate monocation pairs below the DIE of  $\text{CH}_3\text{CN}^{2+}$ .

KERs for the three-body dissociation reactions of  $\text{CH}_3\text{CN}^{2+}$  can be determined in the same way as for the two-body dissociations. However, to simulate the form of the  $t_1$ - $t_2$  spectrum for a three-body dissociation we require the dissociation mechanism. Information on the dissociation pathway can often be extracted from  $p_r$  the gradient of the peak in the pairs spectrum, as discussed above. Consider the dissociation of  $\text{CH}_3\text{CN}^{2+}$  into  $\text{CN}^+ + \text{CH}_2^+ + \text{H}$ , in principle the following dissociation pathways are possible:



By comparing  $p_r$  to the experimentally measured peak gradient it is often possible to infer which mechanism is occurring. For example, The  $\text{CN}^+ + \text{CH}_2^+ + \text{H}$  peak has an experimental gradient of  $-0.89 \pm 0.02$ . Equations (7) – (10) present possible fragmentation pathways from  $\text{CH}_3\text{CN}^{2+}$  to  $\text{CN}^+ + \text{CH}_2^+ + \text{H}$  and the  $p_r$  for each pathway. Clearly, mechanism 2, formation of  $\text{CH}_2^+$  *via* dissociation of a nascent  $\text{CH}_3^{+*}$  ion gives the best agreement between experimental data and model pathway. Similar calculations were repeated for all the observed three-body decays, where the peak intensity was large enough to allow extraction of reliable peak gradients, and KERs were fitted using the appropriate mechanism. Table 3 lists the three-body decays for which this analysis was applied, giving the proposed pathway and fitted KER.

The experimental peak gradient for the dissociation of  $\text{CH}_3\text{CN}^{2+}$  into  $\text{C}_2\text{N}^+ + \text{H}_2^+$  shows some intriguing behaviour. At low electron energies the peak gradient  $p_r$  for this fragmentation is  $-0.56 \pm 0.06$ , close to the value of  $p_r = -2/3$  predicted for sequential dissociation *via*  $\text{C}_2\text{N}^+ + \text{H}_3^{+*}$ . However, as the electron energy is increased  $p_r$  also increases, reaching a value of  $-0.85 \pm 0.06$  at 200 eV. This second value is closer to the value of  $-1.03$  predicted for dissociation *via*  $\text{C}_2\text{HN}^{+*} + \text{H}_2^+$ . This increase in experimental gradient with increasing ionization energy suggests that the main mechanism forming  $\text{C}_2\text{N}^+ + \text{H}_2^+$  changes as the ionizing energy is increased. It is possible that the secondary fragmentation of the  $\text{H}_3^{+*}$  ion gets faster as the internal energy deposited in this nascent fragment increases with increasing electron energy. If the dissociation of the  $\text{H}_3^+$  ion starts to occur in the Coulomb field of  $\text{C}_2\text{N}^+$  the peak gradient will move towards  $-1$ . Alternatively, as the electron energy is increased, more internal energy will also be deposited into the nascent  $\text{C}_2\text{HN}^+$  formed by the two-

body dissociation from  $\text{CH}_3\text{CN}^{2+}$  to  $\text{C}_2\text{HN}^+ + \text{H}_2^+$ . This extra internal energy will lead to an increase in the rate of fragmentation of  $\text{C}_2\text{HN}^+$  to  $\text{C}_2\text{N}^+$  and, hence, an increase in the contribution of this decay pathway to the  $\text{C}_2\text{N}^+ + \text{H}_2^+$  channel, moving the gradient towards -1. In support of this explanation, a corresponding and complementary change in the mechanism for the production of  $\text{C}_2\text{HN}^+ + \text{H}^+$  is also observed. Specifically, the contribution of the decay of a nascent  $\text{H}_2^{+*}$  product to the  $\text{C}_2\text{HN}^+ + \text{H}^+$  channel increases with increasing electron energy. This observations shows that extra internal energy is deposited into the  $\text{H}_2^+$  formed in the nascent  $\text{C}_2\text{HN}^+ + \text{H}_2^+$  fragmentation, leading to an increased probability of  $\text{H}_2^+$  then dissociating into  $\text{H}^+$ .

Ruhl *et al* used He(II) radiation to examine the double photoionization of  $\text{CH}_3\text{CN}$  focussing on charge-separating processes.[35] Ruhl *et al* determined mechanisms and KERs for the observed two and three-body dissociations of  $\text{CH}_3\text{CN}^{2+}$ . The same reactions that we observe following electron double ionization of  $\text{CH}_3\text{CN}$  are also seen in the work of Ruhl *et al* following photon ionization. For the two-body dissociations of  $\text{CH}_3\text{CN}^{2+}$ , the KERs derived from the two experiments are very similar, agreeing within their mutual error limits. (Table 2) However, the KERs derived for the three-body decays, from the photoionization experiments [35] and the electron ionization experiments reported here, differ more significantly.(Table 3) Specifically, the KERs from electron ionization are often several electron Volts higher than those from photoionization. This difference in KERs is not due different mechanisms operating in the decay of the  $\text{CH}_3\text{CN}^{2+}$  ion generated by electrons or photons as, reassuringly, both experiments extract identical three-body dissociation mechanisms. Almost certainly, the higher KERs extracted from our electron ionization experiments arise from differences in the ionizing energy. In this work, most of the three-body KERs were extracted from spectra recorded at electron energies of 65 eV and above, the lowest electron energies for which we could obtain reliable analysis of a given dissociation reaction, compared with the 40.8 eV photon energy Ruhl *et al* used for their experiments. These higher electron energies allow the formation of precursor  $\text{CH}_3\text{CN}^{2+}$  ions in higher-lying electronic states, in addition to the states closer to the DIE populated in the photon ionization experiments. If these higher-lying  $\text{CH}_3\text{CN}^{2+}$  states correlate to the same product asymptotes as the lower-lying dication states, which it appears they do, then they would dissociate to give products with more kinetic energy, as we observe. Hence, in Table 3, we only report a precursor energy for the  $\text{CHCN}^+ + \text{H}^+$  channel, which we can analyse reliably at an electron energy of 50 eV. The associated precursor energy of 37.0 eV lies markedly above the ground state of  $\text{CH}_3\text{CN}^{2+}$ , which is not surprising as significantly more internal energy will be required to allow the rupture of two chemical bonds.

Triple ionization of  $\text{CH}_3\text{CN}$  is a very minor contributor to the ion yield at all electron energies investigated in this work; significant numbers of triples are only recorded above 120 eV. Even at an electron energy of 200 eV, triple ionization processes make up less than one percent of the measured relative PICS. This observation is in agreement with studies of the electron ionization for similar

organic molecules (such as methanol) which also show such small amounts of triple ionization in this electron energy range.[39]

## 4.2 Photon Ionization

The list of ions (given above in Section 3) we observe in our photoionization experiments are very similar to those we observe in the electron impact experiments. In Table 1 we list the ions we detect that are formed by double photoionization at 42 eV photon energy, while a list of the observed photoion-pairs are given in the SI (Table S2). The lists of ions originating from double ionization are nearly identical for the electron and photon experiments. The only differences are that  $C^{2+}$  is a very weak signal in the electron ionization experiments but not observed in the photoionization experiments; conversely  $N^{2+}$  is a weak signal in the photon experiments and not in the electron ionization data. We note the  $C_2H_2^+/CN^+$  and  $C_2N^+$  ions have markedly higher relative intensities from photoionization than from electron ionization. This is probably due to the difference in the ionizing energy for the data in Table 1 (42 eV for photons versus 200 eV for electrons) leading to less fragmentation in the photon-induced spectra.

Figure 6 shows RII extracted from PEPICO spectra recorded following the ionization of  $CH_3CN$  with photons of energies from 20 – 36 eV. For clarity, only results for selected ions are plotted in Figure 6, but the selection is such that Figure 6a-c are representative for all ions detected over this energy range. Figure 6a shows the yield of  $CH_2^+$  and exhibits a clear peak centred at 24.9 eV and a smaller one at 21.7 eV, both peaks superimposed on non-zero background. This background signal is most likely due to detection of high energy electrons (those directed directly towards the detector) from the population of lower lying states of  $CH_3CN^+$ . The peak at 24.9 eV is also observed in the RII of  $CH^+$ ,  $C_2N^+$ ,  $C_2H_2^+$  and  $C_3HN^+$ , whilst the smaller peak is seen for  $CH_3^+$ ,  $C_2N^+$  and  $C_2HN^+$ . Holland and Karlsson studied the valence ionization of  $CH_3CN$  over a range of photon energies,[16] and observed both of these peaks. Holland and Karlsson assigned the larger peak at 25 eV as the  $^2A_1$  state of  $CH_3CN^+$ , arising from ionization from the  $5a_1$  orbital.

Figure 6(b) shows the RII for formation of  $C_2H^+$  from 26 – 35 eV. In this ion yield there is an increase in signal from around 27 eV, plateauing at ~32 eV; there is also a sharp peak at 32.6 eV. It is noticeable that compared to the  $CH_2^+$  yield there is no background until the onset in signal at 27 eV, indicating that this ion is not formed significantly by single ionization at low ionizing energies. The double ionization energy of  $CH_3CN$ , as discussed above, is close to 33.5 eV which means the significant signals for  $C_2H^+$  below the DIE are not from direct double ionization processes but are most likely due to the formation of  $CH_3CN^+$  in electronically excited states which are part of one or more Rydberg series that converge on low lying states of the dication. Indeed, such states have been implicated above in producing ion pairs below the double ionization threshold. The marked increase in the  $C_2H^+$  signal just below 33.3 eV, where the density of such Rydberg states should increase, is

in accord with this assignment. The likely assignment of the sharp features is to such excited monocation states (or even super-excited neutral states) which are initially populated *en route* to the formation of  $C_2H^+$ .

The RII for  $C_2H_2N^+$  from 26 – 35 eV is shown in Figure 66c. In this spectrum there is a weak onset in signal, with a distinct superimposed structures, above 33 eV. The  $CH_3CN^{2+}$  and  $CH_2CN^{2+}$  ions we detect also show similar behaviour. To determine the threshold in this spectrum the fitting method described above was applied to the ion intensities for both  $C_2H_2N^+$  and  $CH_2CN^{2+}$ , as these ion signals were large enough to support such analysis. This fitting gave values of  $E_A$  of  $33.2 \pm 1.0$  eV and  $32.7 \pm 1.0$  eV for  $C_2H_2N^+$  and  $CH_2CN^{2+}$  respectively. These thresholds are close to the DIE of 33.3 eV measured by Bayliss *et al.* The simplest explanation of these thresholds is that there are dissociative channels open for the  $CH_3CN^{2+}$  dication to these products at energies close to the double ionization energy. Again, the sharp structures are likely due to the population of specific neutral or monocationic states *en route* to the formation of these ions. More generally, the structures in these first photoion yields indicate such spectra are worthy of more detailed investigation, in a study with access to greater beamtime, to probe in more detail the electronic structure of  $CH_3CN^{2+}$ .

PEPIPICO spectra were recorded from 34 – 42 eV photon energy. A list of the ion pairs observed in these spectra is given in Table S2; this list is very similar to the ion pairs detected in our electron ionization experiments. We note that in the photoionization experiments the pairs intensity is concentrated in a smaller subset of the observed dication dissociation reactions than in the electron ionization data (Tables S1 and S2). The PEPIPICO spectra reveal the main ion-pair channels all involve the formation of  $H^+$ , accounting for 77 % of detected events. In the photoionization data the most intense ion-pair is the two-body dissociation of  $CH_3CN^{2+}$  to  $H^+$  and  $CH_2CN^+$ . Rühl *et al* saw a similar percentage of pair events involving  $H^+$  (67 %) at a photon energy of 40.8 eV, while at 200 eV electron energy we observe that 71 % of events include the formation of  $H^+$ . Due to the low count rate for formation of ion pairs below 34 eV, coupled with the high false coincidence background inherent in the use of a quasi-continuous source such as a synchrotron, it was impossible to extract reliable thresholds for the ion-pair processes observed in the PEPIPICO spectra. Overall we note there is a striking similarity between the ionization behaviour we observe in the photon and electron ionization experiments.

In the literature, comparison of the fragmentation pattern observed following photoionization of  $CH_2Cl_2$ , with that recorded following ionization of the same molecule by proton impact, has indicated that similar mass spectra are observed at similar values of the momentum transferred in the ionizing collision (photon *vs.* proton).[60] Such a model explains the greater fragmentation observed at lower (200keV *vs.* 2 MeV) proton impact energies and at higher photon energies (12 eV *vs.* 90 eV). Using the model employed by Alcantara *et al.*,[60], the momentum transfer appears significantly different between the photoionization and electron ionization cases in our experiments. It is perhaps not

surprising that such a model, based on a classical framework, does not work well at our relatively low electron energies, where the incident electron has comparable velocities to the valence electrons. However, the similarity in the current work between the fragmentation patterns following ionization with 200 eV electrons and 40 eV photons, is in general accord with the, now well-accepted, observation that significantly higher electron energies than photon energies are required to generate comparable double ionization yields.[61]

## 5. Conclusions

The ionization of CH<sub>3</sub>CN has been studied, using both electrons and photons as the ionizing agent, using 2D TOF coincidence spectrometry. Following electron ionization, both partial ionization cross sections and relative precursor-specific partial ionization cross-sections for the formation of all detected positive ion fragments have been determined over an electron energy range from 30 – 200 eV. These cross sections, and the ionization thresholds we determine, fully characterize, the formation of cations from CH<sub>3</sub>CN over this electron energy range. The two- and three-body dissociations of CH<sub>3</sub>CN<sup>2+</sup> have also been investigated revealing that a large number of charge-separating fragmentation pathways are accessible to the low-lying electronic states of the CH<sub>3</sub>CN<sup>2+</sup> dication.

The identities of the cations formed, and their relative intensities, via photoionization are very similar to those formed by electron ionization. The photoionization results reveal a significant contribution to the ion yields close to, and above, the double ionization potential from the population of highly-excited states of the monocation or neutral molecule.

## Acknowledgements

We wish to acknowledge the SLS for providing beamtime and Andras Bodi for assistance in acquiring the photon ionization data. MAP wishes to thank COST action CM0805 “The Chemical Cosmos” for providing funding for a short-term scientific mission. We thank the EPSRC for financial support in the form of a studentship and equipment grants.

## References

- [1] P.M. Solomon, K.B. Jefferts, A.A. Penzias and R.W. Wilson *Astrophysical Journal* **168** (1971) L107
- [2] B.E. Turner, P. Friberg, W.M. Irvine, S. Saito and S. Yamamoto *Astrophys. J.* **355** (1990) 546
- [3] R.L. Hudson and M.H. Moore *Icarus* **172** (2004) 466
- [4] E. Murad, W. Swider, R.A. Moss and S. Toby *Geo. Res. Letts.* **11** (1984) 147
- [5] G. Moneti, G. Pieraccini, D. Favretto and P. Traldi *J. Mass Spec.* **34** (1999) 1354
- [6] S. Hamm, J. Hahn, G. Helas and P. Warneck *Geo. Res. Letts.* **11** (1984) 1207
- [7] H. Bohringer and F. Arnold *Nature* **290** (1981) 321
- [8] H. Schlager and F. Arnold *Planet Space Sci.* **33** (1985) 1363
- [9] M.A. Cordiner, M.Y. Palmer, C.A. Nixon, P.G.J. Irwin, N.A. Teanby, S.B. Charnley, M.J. Mumma, Z. Kisiel, J. Serigano, Y.J. Kuan, Y.L. Chuang and K.S. Wang *Astrophys. J. Lett.* **800** (2015) 7 L14
- [10] S.M. Abbott, J.B. Elder, P. Španěl and D. Smith *Int. J. Mass Spec.* **228** (2003) 655
- [11] C.K. Van Pelt, B.K. Carpenter and J.T. Brenna *J. Am. Mass Spec. Soc.* **10** (1999) 1253
- [12] S.P. Alves, C. Tyburczy, P. Lawrence, R.J.B. Bessa and J.T. Brenna *Rap. Commun. Mass Spec.* **25** (2011) 1933
- [13] M. Schwell, H.-W. Jochims, H. Baumgartel and S. Leach *Chem. Phys.* **344** (2008) 164
- [14] S. Leach, M. Schwell, S. Un, H.-W. Jochims and H. Baumgartel *Chem. Phys.* **344** (2008) 147
- [15] C.-K. Huang, I.-F. Lin and S.-Y. Chiang *Chem. Phys. Lett.* **440** (2007) 51
- [16] D.M.P. Holland and L. Karlsson *J. Elec. Spec. Rel. Phenon.* **150** (2006) 47
- [17] D.M. Rider, G.W. Ray, E.J. Darland and G.E. Leroi *J. Chem. Phys.* **74** (1981) 1652
- [18] V.H. Dibeler and S.K. Liston *J. Chem. Phys.* **48** (1968) 4765
- [19] J. Yang, C. Zhou and Y. Mo *J. Phys. Chem. A* **109** (2005) 9964
- [20] T. Horio, R. Maruyama, N. Kishimoto and K. Ohno *Chem. Phys. Lett.* **384** (2004) 73
- [21] M. Yamazaki, S. Maeda, N. Kishimoto and K. Ohno *J. Chem. Phys.* **117** (2002) 5707
- [22] T. Pasinszki, H. Yamakado and K. Ohno *J. Phys. Chem.* **99** (1995) 14678
- [23] C.A. McDowell and J.W. Warren *Trans. Faraday Soc.* **48** (1952) 1084
- [24] W. Heerma, J.J. Deridder and G. Dijkstra *Org. Mass Spec.* **2** (1969) 1103
- [25] J.L. Franklin, Y. Wada, P. Natalis and P.M. Hierl *J. Phys. Chem.* **70** (1966) 2353
- [26] P.W. Harland and B.J. McIntosh *Int. J. Mass Spec. Ion Proc.* **67** (1985) 29
- [27] E.K. Chess, R.L. Lapp and M.L. Gross *Org. Mass Spec.* **17** (1982) 475
- [28] Y. Boran, A.A. Kolomenskii, M. Sayrac, N. Kaya, H.A. Schuessler and J. Strohaber *J. Phys. B* **50** (2017) 10 135003
- [29] R.R. Rye and J.E. Houston *J. Chem. Phys.* **75** (1981) 2085
- [30] E. Kukk, R. Sankari, M. Huttula, S. Mattila, E. Itälä, A. Sankari, H. Aksela and S. Aksela *Int. J. Mass Spec.* **279** (2009) 69
- [31] C. Harada, S. Tada, K. Yamamoto, Y. Senba, H. Yoshida, A. Hiraya, S. Wada, K. Tanaka and K. Tabayashi *Radiation Physics and Chemistry* **75** (2006) 2085
- [32] S. Pilling, D.P.P. Andrade, R. Neves, A.M. Ferreira-Rodrigues, A.C.F. Santos and H.M. Boechat-Roberty *Mon. Not. R. Astron. Soc.* **375** (2007) 1488
- [33] M.A. Bayliss, S.E. Silcocks, F.M. Harris, S.R. Andrews and D.E. Parry *Int. J. Mass Spec. Ion Proc.* **163** (1997) 121
- [34] J.H.D. Eland *Rap. Commun. Mass Spec.* **10** (1996) 1560
- [35] E. Ruhl, S.D. Price, S. Leach and J.H.D. Eland *Int. J. Mass Spec. Ion Proc.* **97** (1990) 175
- [36] S.J. King and S.D. Price *J. Chem. Phys.* **127** (2007) 174307
- [37] N.A. Love and S.D. Price *Phys. Chem. Chem. Phys.* **6** (2004) 4558
- [38] D.M. Curtiss and J.H.D. Eland *Int. J. Mass Spec. Ion Phys.* **63** (1985) 241
- [39] K.M. Douglas and S.D. Price *J. Chem. Phys.* **131** (2009) 224305

- [40] L. J. Frasinski, M. Stankiewicz, P. A. Hatherly and K. Codling *Meas. Sci. Technol.* **3** (1992) 1188
- [41] T. Fiegele, G.T. Hanel, I. M. Lezius and T.D. Märk *J. Phys. B* **33** (2000) 4263
- [42] J.H.D. Eland *Mol. Phys.* **61** (1987) 725
- [43] S. Hsieh and J.H.D. Eland *J. Phys. B* **30** (1997) 4515
- [44] J.H.D. Eland *Chem. Phys. Lett.* **203** (1993) 353
- [45] M. Johnson, A. Bodi, L. Schulz and T. Gerber *Nuc. Instrum. Meths. Phys. Res. A* **610** (2009) 597
- [46] A. Bodi, M. Johnson, T. Gerber, Z. Gengeliczki, B. Sztáray and T. Baer *Rev. Sci. Instrum.* **80** (2009) 034101
- [47] A. Bodi, B. Sztáray, T. Baer, M. Johnson and T. Gerber *Rev. Sci. Instrum.* **78** (2007) 084102
- [48] M. Johnson, A. Bodi, L. Schulz and T. Gerber *Nuc. Instrum. Meths. Phys. Res. A* **610** (2009) 597
- [49] S.J. King and S.D. Price *Int. J. Mass Spec.* **272** (2008) 154
- [50] S.J. King and S.D. Price *Int. J. Mass Spec.* **277** (2008) 84
- [51] S.J. King and S.D. Price *J. Chem. Phys.* **134** (2011) 074311
- [52] M.D. Ward, S.J. King and S.D. Price *J. Chem. Phys.* **134** (2011) 024308
- [53] R. Feifel, J.H.D. Eland and D. Edvardsson *J. Chem. Phys.* **122** (2005) 144308
- [54] J.H.D. Eland *Chem. Phys.* **294** (2003) 171
- [55] J.H.D. Eland, P. Lablanquie, M. Lavollee, M. Simon, R.I. Hall, M. Hochlaf and F. Penent *J. Phys. B* **30** (1997) 2177
- [56] H. Aksela, S. Aksela, A.N. Debrito, G.M. Bancroft and K.H. Tan *Phys. Rev. A* **45** (1992) 7948
- [57] P. Morin and I. Nenner *Phys. Rev. Lett.* **56** (1986) 1913
- [58] S.J. Schaphorst, C.D. Caldwell, M.O. Krause and J. Jimenezmier *Chem. Phys. Lett.* **213** (1993) 315
- [59] J.D. Fletcher, M.A. Parkes and S.D. Price *J. Chem. Phys.* **138** (2013) 184309
- [60] K.F. Alcantara, W. Wolff, A.H.A. Gomes, L. Sigaud, S. Soriano, V. Oliveira, A.B. Rocha and A.C.F. Santos *J. Phys. B* **44** (2011) 9 165205
- [61] B.P. Tsai and J.H.D. Eland *Int. J. Mass Spec. Ion Proc.* **36** (1980) 143
- [62] S. Lias, J. Bartmess, J. Liebman, J. Holmes, R. Levin and W. Mallard in *NIST Chemistry WebBook, NIST Standard Reference Database Number 69* Mallard W, Linstrom P (eds), (Retrieved 2017), National Institute of Standards and Technology, Gaithersburg MD, 20899 (<http://webbook.nist.gov>)

## Tables

Table 1: Appearance energies (thresholds,  $E_A[\text{EI}]$ ) for ions formed from electron double ionization of  $\text{CH}_3\text{CN}$ . Representative ion intensities from double ionization are also reported at 200 eV electron energy and at 42 eV photon energy. The intensity is a percentage of all observed ions formed from double ionization. An asterisk (\*) indicates that, in the photoionization data, the ion is not observed at 42 eV but is observed at lower photon energies.

Ion	$E_A[\text{EI}] / \text{eV}$	Intensity (%) electron ionization (200 eV)	Intensity (%) photon ionization (42 eV)
$\text{H}^+$	42.3 (0.8)	36.0	39.5
$\text{H}_2^+$	42.3 (0.5)	1.7	2.6
$\text{H}_3^+$	43.3 (0.9)	0.1	0.3
$\text{C}^+$	51.4 (1.0)	7.0	1.5
$\text{CH}^+$	36.9 (0.7)	4.5	2.0
$\text{CH}_2^+$	46.5 (1.0)	10.3	3.2
$\text{CH}_3^+$	43.0 (1.0)	1.2	1.6
$\text{C}_2^+$	63.3 (0.5)	3.6	*
$\text{C}_2\text{H}^+$	54.2 (1.0)	3.2	*
$\text{C}_2\text{H}_2^+ / \text{CN}^+$	47.5 (0.8)	6.2	1.4
$\text{C}_2\text{H}_3^+ / \text{HCN}^+$	43.7 (1.1)	2.3	1.7
$\text{CH}_2\text{N}^+$	39.2 (1.0)	3.2	3.6
$\text{CH}_3\text{N}^+$	36.0 (10.3) <sup>a</sup>	0.01	0.1
$\text{C}_2\text{N}^+$	48.4 (0.5)	6.4	17.2
$\text{CHCN}^+$	43.7 (0.6)	5.4	8.0
$\text{CH}_2\text{CN}^+$	38.9 (0.8)	8.1	15.6
$\text{C}^{2+}$	133 (5) <sup>a</sup>	<0.01	*
$\text{N}^{2+}$	-	-	0.02
$\text{C}_2\text{N}^{2+}$	46.2 (1.6)	0.1	*
$\text{CHCN}^{2+}$	47.4 (1.2)	0.1	0.03
$\text{CH}_2\text{CN}^{2+}$	38.2 (0.4)	0.8	1.5
$\text{CH}_3\text{CN}^{2+}$	34.1 (0.8)	0.02	0.02

a This channel is very weak, hence, the significant uncertainty in the threshold determination.

Table 2: Kinetic energy releases (KERs) for two-body fragmentation of  $\text{CH}_3\text{CN}^{2+}$  formed by electron ionization at the electron energies listed. The dicationic precursor state energy ( $E_p$ ) provides an estimate of the energy of the  $\text{CH}_3\text{CN}^{2+}$  state from which dissociation occurs. See text for details.

Ion Pair	Electron Energy / eV	KER / eV ( $\pm 0.5$ eV)	Lit. Value / eV <sup>a</sup>	$E_p$ / eV <sup>b</sup> ( $\pm 0.5$ eV)
$\text{CH}_2\text{CN}^+ + \text{H}^+$	45	3.0	3.3	33.6
$\text{CHCN}^+ + \text{H}_2^+$	55	3.5	3.3	37.9
$\text{CH}_2\text{N}^+ + \text{CH}^+$	50	4.5	4.6	31.2
$\text{CHN}^+ + \text{CH}_2^+$	50	4.5	4.6	34.0
$\text{CN}^+ + \text{CH}_3^+$	55	4.5	4.0	30.9

- a Taken from ref [35]  
 b Thermochemistry taken from [62]

Table 3: Kinetic energy releases (KERs) for three-body fragmentation of  $\text{CH}_3\text{CN}^{2+}$  following ionization at the stated electron energies, and the calculated and experimental values of the gradient of the associated peak in the pairs spectrum. The precursor state energy ( $E_p$ ) represents the energy of the  $\text{CH}_3\text{CN}^{2+}$  state from which the dissociation occurs. See text for details.

Ion Pair	Proposed Pathway	Peak Gradient		Electron Energy / eV	Kinetic energy release		
		Calc.	Expt.		KER / eV $\pm 0.5$ eV	Lit <sup>a</sup> / eV	$E_p$ / eV <sup>b</sup>
$\text{CHCN}^+ + \text{H}^+$	$\text{C}_2\text{HN}^+ + \text{H}_2^+$	-0.5	-0.46(2)	50	3.0	3.3	37.0
$\text{C}_2\text{N}^+ + \text{H}_2^+$	$\text{C}_2\text{N}^+ + \text{H}_3^+$	-0.7	-0.81(2)	65	4.0	1.3	-
$\text{CH}_2\text{N}^+ + \text{C}^+$	$\text{CH}_2\text{N}^+ + \text{CH}^+$	-0.9	-0.94(1)	85	5.0	2.4	-
$\text{CHN}^+ + \text{CH}^+$	$\text{CH}_2\text{N}^+ + \text{CH}^+$	-0.9	-0.93(2)	85	4.0	2.5	-
$\text{CN}^+ + \text{CH}_2^+$	$\text{CN}^+ + \text{CH}_3^+$	-0.9	-0.89(2)	55	5.0	2.5	-

- a Taken from ref [35]  
 b Thermochemistry taken from [62]

## Figures

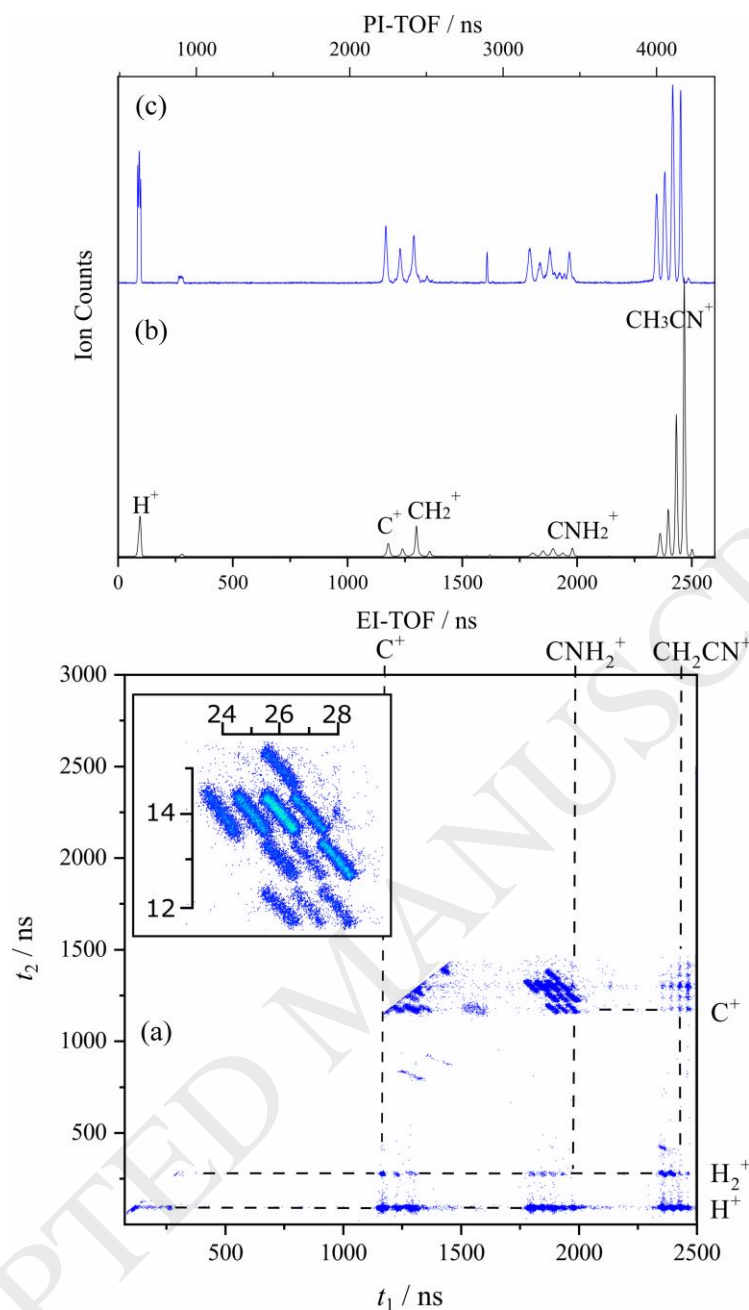


Figure 1 Representative pairs spectrum and mass spectra recorded following ionization of  $\text{CH}_3\text{CN}$ . A section of the raw pairs spectrum (a) taken at 200 eV electron energy is shown as a spot plot, where a spot indicates a cell in the array that contains at least one count; such a presentation emphasises weaker peaks. The inset, on a linear intensity scale, is an enlargement of a group of the strongest coincidence signals, labelled with axes indicating the fragment mass. This inset clearly shows the characteristic gradient (slope) of the pairs signals for the individual dissociation reactions. The mass spectrum (b) is a corresponding “singles” spectrum recorded at 200 eV electron energy. Mass spectrum (c), for comparison, is a singles spectrum recorded at 41 eV photon energy. See text for details.

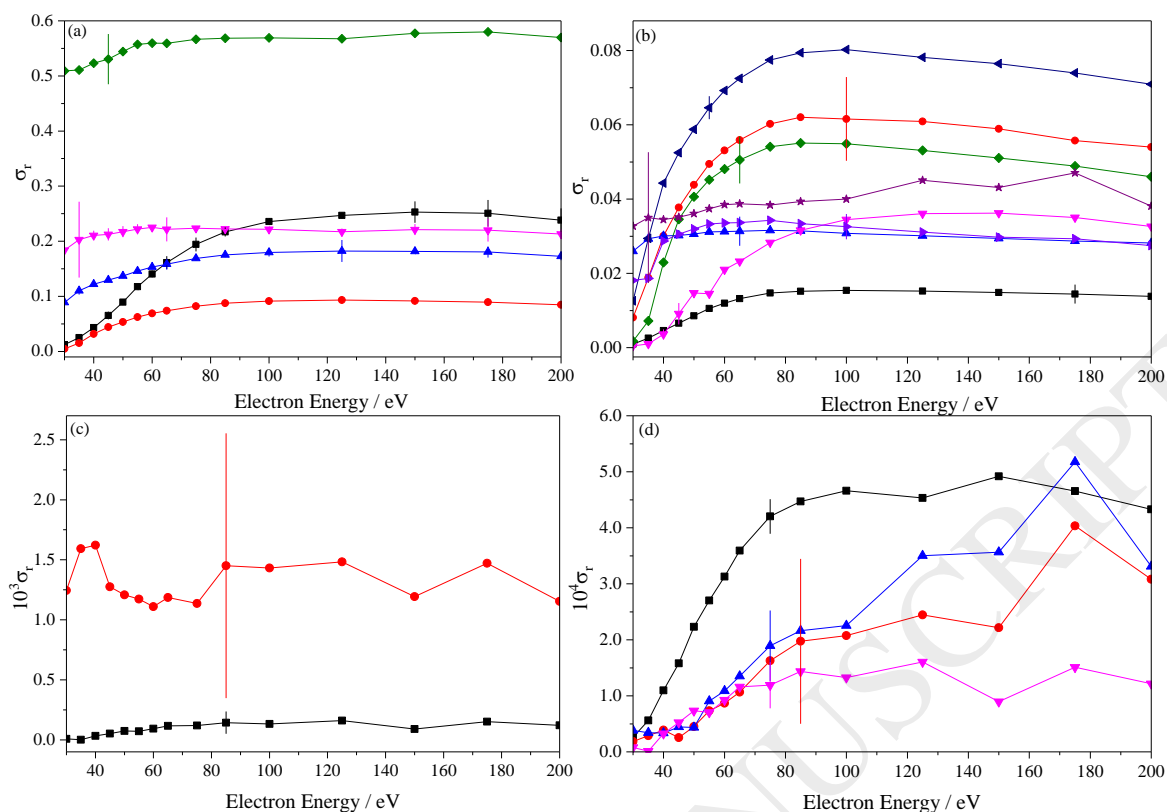


Figure 2: Relative partial ionization cross-sections  $\sigma_r[X^{m+}]$  for forming (a)  $H^+$  (■),  $C^+$  (●),  $CH_2^+/N^+$  (▲),  $CHCN^+$  (▼) and  $CH_2CN^+$  (◆) (b)  $H_2^+$  (■),  $CH^+$  (●),  $CH_3^+/NH^+$  (▲),  $C_2^+$  (▼),  $C_2H^+$  (◆),  $C_2H_2^+/CN^+$  (◀),  $C_2H_3^+/HCN^+$  (▶) and  $H_2CN^+$  (★) (c)  $CH_3CN^{2+}$  (■) and  $H_3CN^+$  (●) (d)  $H_3^+$  (■),  $C_2N^+$  (●),  $CHCN^{2+}$  (▲) and  $CH_3CN^{2+}$  (▼) following electron ionization of  $CH_3CN$  from 30 - 200 eV electron energy. The error bars shown represent 4 standard deviations ( $\pm 2sd$ ) in (a), 6 standard deviations ( $\pm 3sd$ ) in (b) and 2 standard deviations ( $\pm 1sd$ ) in (c) and (d). These error bars are determined from four separate measurements and are indicative of the errors across the energy range. Values and uncertainties for every data point are given in the tables of data provided in the supplementary information.

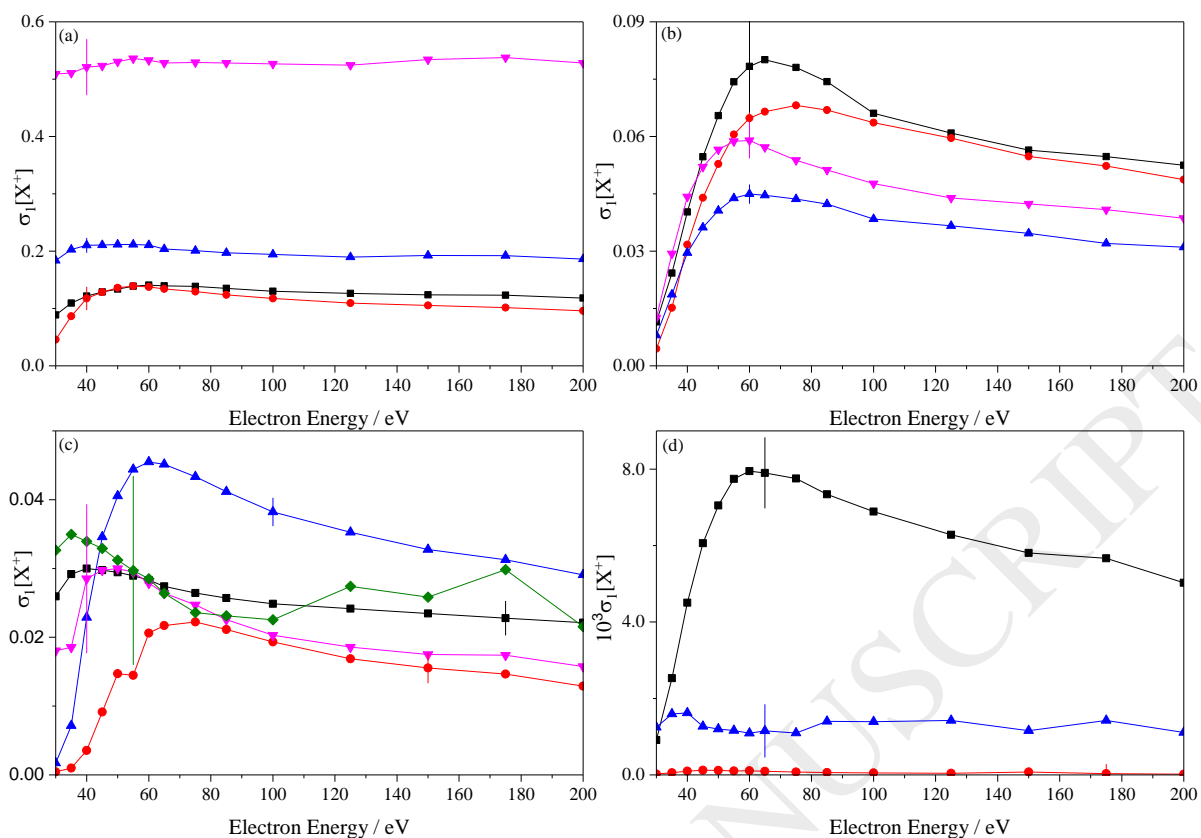


Figure 3: Relative partial precursor-specific cross-sections  $\sigma_1[X^+]$  for forming (a)  $\text{CH}_2^+/\text{N}^+$  (■),  $\text{C}_2\text{N}^+$  (●),  $\text{C}_2\text{N}^+$  (▲) and  $\text{CH}_2\text{CN}^+$  (▼) (b)  $\text{H}^+$  (■),  $\text{C}^+$  (●),  $\text{CH}^+$  (▲) and  $\text{C}_2\text{H}_2^+/\text{CN}^+$  (▼) (c)  $\text{CH}_3^+/\text{NH}^+$  (■),  $\text{C}_2^+$  (●),  $\text{C}_2\text{H}^+$  (▲),  $\text{C}_2\text{H}_3^+/\text{CHN}^+$  (▼) and  $\text{CH}_2\text{N}^+$  (◆) (d)  $\text{H}_2^+$  (■),  $\text{H}_3^+$  (●) and  $\text{CH}_3\text{N}^+$  (▲) following single electron-ionization of  $\text{CH}_3\text{CN}$  from 30 - 200 eV. The error bars shown represent 6 standard deviations ( $\pm 3\text{sd}$ ) in (a), 8 standard deviations ( $\pm 4\text{sd}$ ) in (b) and 4 standard deviations ( $\pm 2\text{sd}$ ) in (c) and (d). These error bars are determined from four separate measurements and are indicative of the errors across the energy range. Values and uncertainties for every data point are given in the tables of data provided in the supplementary information.

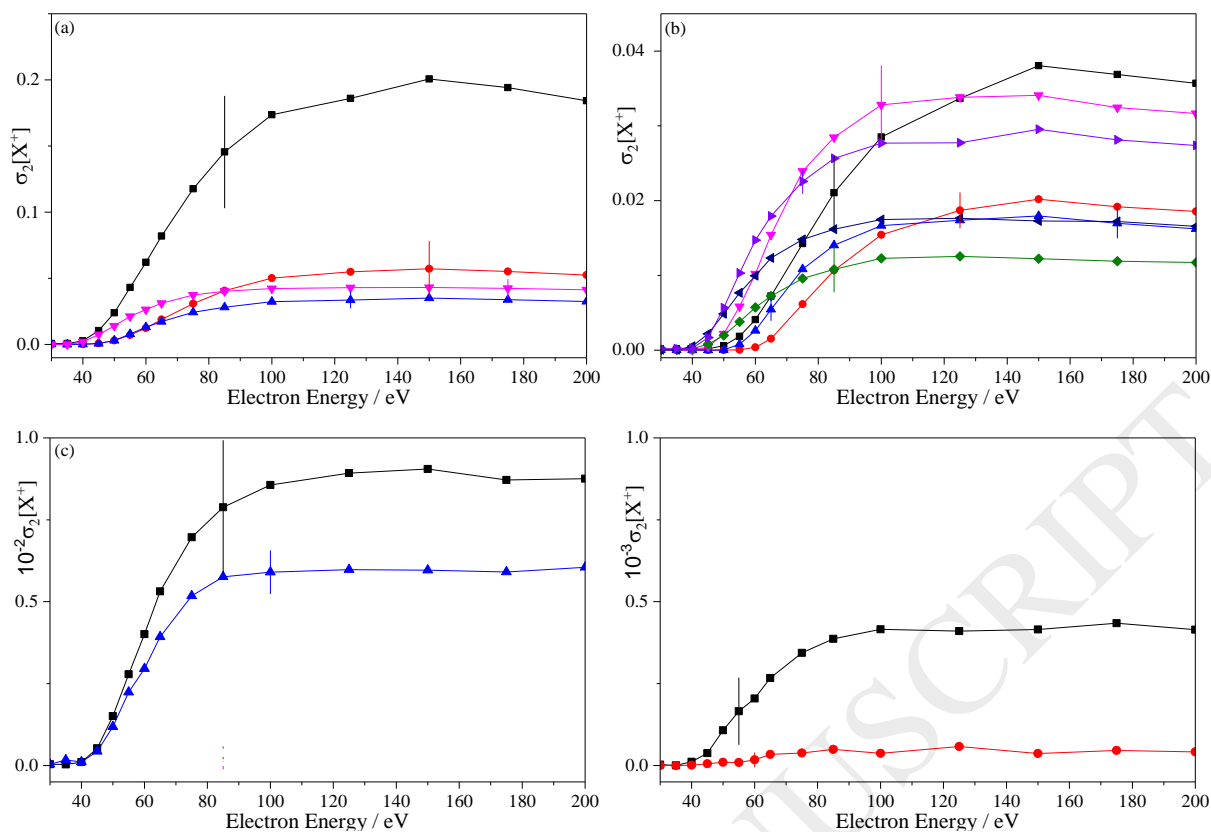


Figure 4: Relative partial precursor-specific cross-sections  $\sigma_2[X^+]$  for forming (a)  $H^+$  (■),  $CH_2^+/N^+$  (●),  $C_2N^+$  (▲) and  $CH_2CN^+$  (▼) (b)  $C^+$  (■),  $C_2^+$  (●),  $C_2H^+$  (▲),  $C_2H_2^+/CN^+$  (▼),  $C_2H_3^+/HCN^+$  (◆),  $CH_2N^+$  (◄) and  $C_2HN^+$  (►) (c)  $H_2^+$  (■) and  $CH_3^+/NH^+$  (▲) (d)  $H_3^+$  (■) and  $CH_3N^+$  (●) following double electron-ionization of  $CH_3CN$  from 30 - 200 eV. The error bars shown represent 6 standard deviations ( $\pm 3sd$ ) in (a), (c) and (d), and 4 standard deviations ( $\pm 2sd$ ) in (b). These error bars are determined from four separate measurements and are indicative of the errors across the energy range. Values and uncertainties for every data point are given in the tables of data provided in the supplementary information.

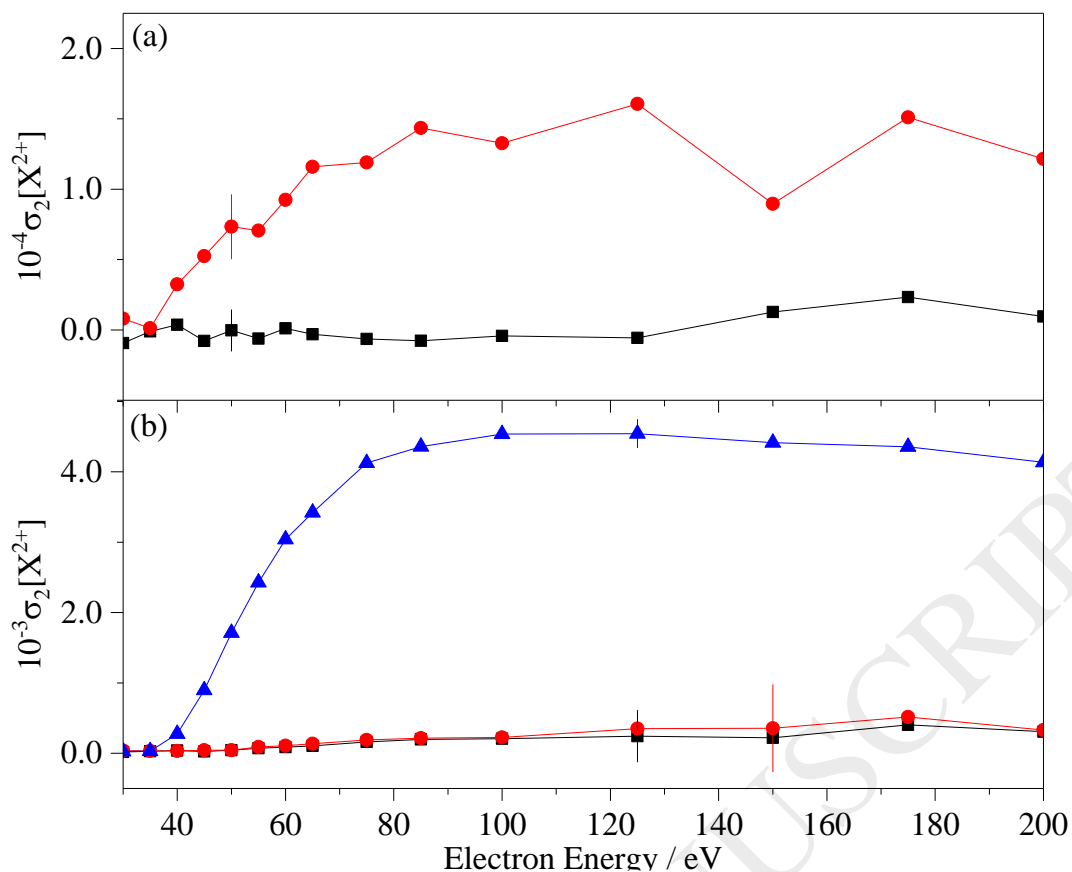


Figure 5: Relative partial precursor-specific cross-sections  $\sigma_2[X^{2+}]$  for forming (a)  $C^{2+}$  (■) and  $CH_3CN^{2+}$  (●) (b)  $C_2N^{2+}$  (■),  $CHCN^{2+}$  (●) and  $CH_2CN^{2+}$  (▲) following double electron-ionization from 30 - 200 eV. The error bars shown represent two standard deviations ( $\pm 1sd$ ) in (a) and four standard deviations ( $\pm 2sd$ ) in (b). These error bars are determined from four separate measurements and are indicative of the errors across the energy range. Values and uncertainties for every data point are given in the tables of data provided in the supplementary information.

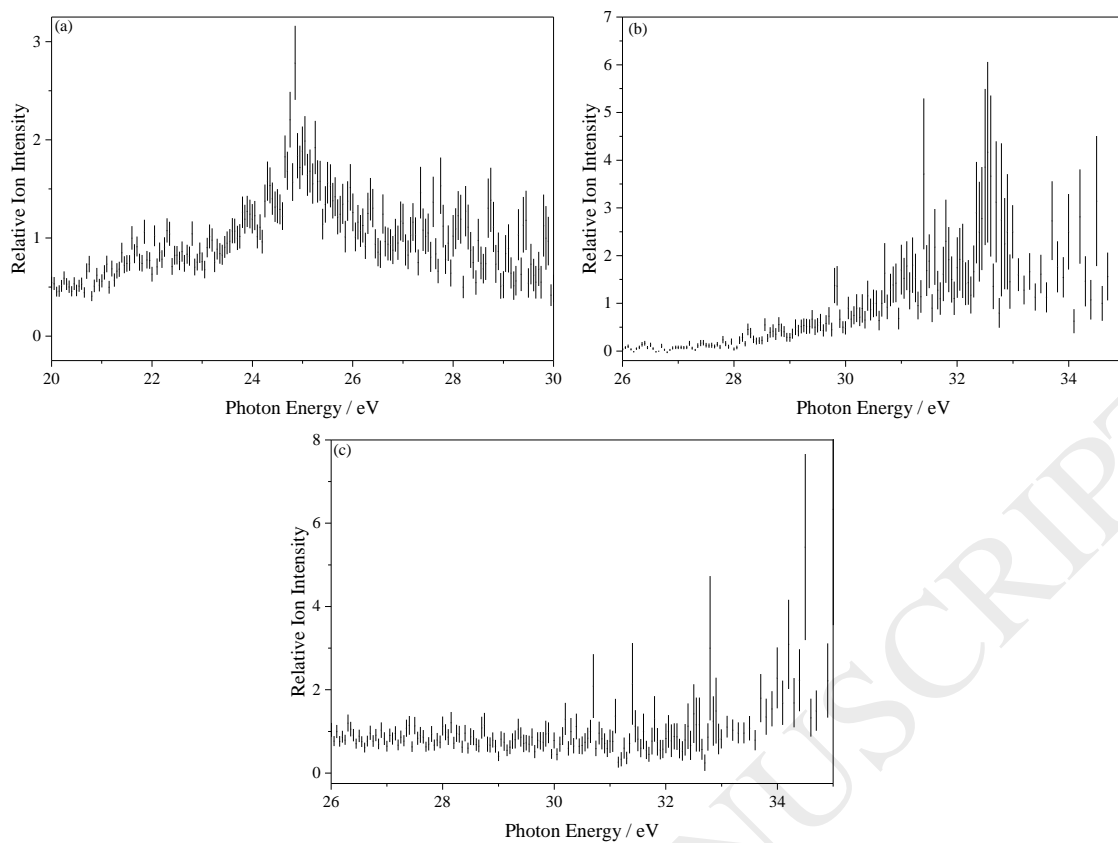


Figure 6: Relative ion intensities for RII) production of (a)  $\text{CH}_2^+$ , (b)  $\text{C}_2\text{H}^+$  and (c)  $\text{CH}_2\text{CN}^+$  from photoionization of  $\text{CH}_3\text{CN}$ .